Polarized single-lobed surface emission in mid-infrared, photonic-crystal, quantum-cascade lasers

Gangyi Xu,[1,3] Yannick Chassagneux,[1] Raffaele Colombelli,[1,4] G. Beaudoin,[2] and I. Sagnes[2]

[1]*Institut d'Electronique Fondamentale, Université Paris Sud, UMR 8622 CNRS, 91405 Orsay, France*
[2]*Laboratoire de Photonique et Nanostructures, LPN/CNRS, Route de Nozay, 91460 Marcoussis, France*
[3]*gangyi.xu@u-psud.fr*
[4]*raffaele.colombelli@u-psud.fr*

We report single-mode, surface-emitting, mid-IR, photonic-crystal (PhC), quantum-cascade lasers with linearly polarized and highly directional single-lobed emission. A metallic square-lattice photonic crystal with elliptical air holes and π phase shift was used as the resonator. The 2D feedback coupling—necessary for the operation of the photonic-crystal resonator—is induced by the mismatch between the modes supported by metalized and nonmetalized regions and yields single-mode output with a side-mode suppression ratio >30 dB. The elliptical air holes modify the relative intensities of the TM field components (H_x and H_y) in the PhC plane, thus yielding linearly polarized emission. The π phase shift allows the system to produce a single-lobed pattern in the far field with a narrow divergence angle ($2.4° \times 1.8°$). The emission is perfectly orthogonal to the device surface, and the maximum operating temperature—still limited by the metallic ohmic losses—is 240 K. © 2010 Optical Society of America

OCIS codes: 140.5965, 050.5298, 140.7270, 140.3300, 050.5080, 230.5440.

Surface-emitting quantum-cascade lasers (QCLs) can find application in the fields of gas sensing, microspectroscopy, and imaging [1–4]. Different methods can be employed to achieve surface emission, including the use of second-order distributed-feedback (DFB) gratings [1,2], and 2D photonic-crystal (PhC) resonators [3,4]. PhC surface-emitting QCLs are typically designed to operate on band-edge states at the Γ point of the photonic band structure [5]. They are very advantageous when there is a need to engineer the device spectral and spatial characteristics. Since the electromagnetic field of the laser modes is delocalized across the entire device surface, single-mode emission with very narrow angular divergence is expected. Careful tailoring of the symmetry and phase of the photonic lattice allows one to control the shape and polarization of the output beam [6–8]. In this Letter, we demonstrate linearly polarized surface emission with an angularly narrow single-lobed far-field pattern in mid-IR QCLs. The devices—which also exhibit single-mode emission—employ metallic PhCs, an approach that has been recently proven highly controllable in the mid-IR [4].

PhC lasers operating on standard triangular or square-lattice PhCs typically exhibit a doughnut-shaped emission pattern in the far field, with a complex polarization pattern. This can be established by investigating the electromagnetic-field distribution in the PhC structure. The modes with lowest loss at the Γ point are antisymmetric, i.e., the TM field—H_x and H_y, as defined in Fig. 1(b)—are antisymmetric with respect to the y and x axes, respectively. The antisymmetric character explains the doughnut-shaped emission [4].

In this work, single-lobed and linearly polarized surface emission is obtained by using a square-lattice
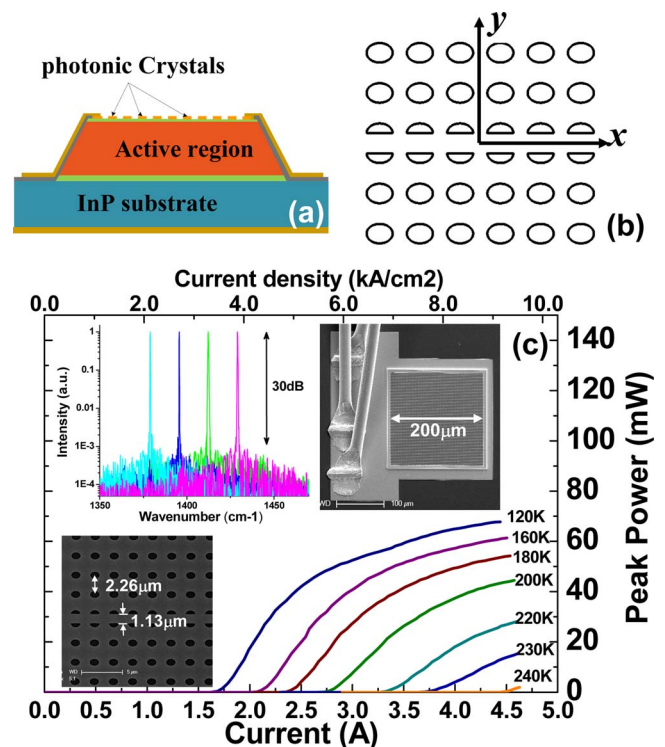

Fig. 1. (Color online) (a) Schematic cross section of a device. (b) Schematic picture of the square-lattice PhC structure. The black curves correspond to the edges of the air holes. A π shift is implemented in the center of the PhC in the y direction. (c) *L-I* curves measured in pulsed mode (50 ns at 84 kHz) at different temperatures. Inset top-left, lasing spectra measured at 78 K in pulsed mode (50 ns at 84 kHz) for devices with different lattice periods a, varying from 2.20 to 2.29 μm in step of 0.03 μm. Inset top-right, SEM picture of a typical device. Inset bottom, SEM image of the central part of a square-lattice PhC.

PhC with elliptical air holes. Figure 1(a) shows a schematic cross section of the device; a metallic PhC is directly "written" on top of the active region. It serves simultaneously as surface-plasmon-carrying layer and as contact for current injection. Figure 1(b) shows a schematic image of the PhC structure; a square lattice of elliptical air holes is implemented in the thin top metallization layer. The elliptical shape of the holes yields a precise control of the output polarization. Furthermore, a π shift phase delay is introduced to obtain single-lobed emission [9].

The laser structure used (F-InP281) is based on InGaAs/AlInAs lattice matched to InP substrate, in a surface-plasmon-waveguide configuration [10]. The active region is designed for nominal emission at λ = 7.5 μm. Details of the material growth are given in [11]. The device processing starts from the definition of the metallic PhC by electron-beam lithography, followed by metal evaporation (Ti/Au, 3/80 nm) and lift-off. Square mesa cavities are then wet etched down to the InP substrate. The side walls of the cavity are passivated with 200-nm-thick Si_xN_y. The top electrode (Ti/Au) is then evaporated to surround and contact the edge of the PhC pattern. After polishing and back-contact deposition, the devices were mounted in a cryostat for characterization. Scanning electron microscope (SEM) images of a typical device and its central part are presented in the insets of Fig. 1(c). The size of the PhC is 200×200 μm. The PhC lattice period (a) varies in a range from 2.20 to 2.29 μm, to overlap the PhC mode frequency with the material gain. The ratio between minor and major axis of the elliptical holes and the filling factor of the PhC were set to 0.75 and 0.14, respectively. The structure parameters used represent a trade-off between the requirements of reduced lasing threshold and good beam quality. Increasing the eccentricity yields a more polarized emission but decreases the cavity quality factor.

Figure 1(c) (top left inset) shows the lasing spectra of four devices with different lattice periods at 78 K. Single-mode emission with a side-mode suppression ratio of >30 dB is observed. The emission wavelength is lithographically tunable in a wide range of ~260 nm. It is single mode for all injected currents, operation temperatures, and photonic lattice periods explored. The light-current characteristics of a typical device at different temperatures are reported in Fig. 1(c). The threshold current density (J_{th}) at 120 K is 3.3 kA/cm^2, and it increases to 9.1 kA/cm^2 at 240 K, the maximum operating temperature (T_{max}). The peak output power reaches 68 mW at 120 K and decreases to 2 mW at 240 K. The performance (J_{th} and T_{max}) are comparable to standard Fabry–Perot lasers fabricated with the same material.

Figures 2(a) and 2(b) show two orthogonally polarized far-field patterns of a typical device. The definition of the angular coordinates, θ_x and θ_y, in the far field is given in the inset of Fig. 2. A grating polarizer is placed in front of an LN-cooled HgCdTe detector that is scanned at a constant distance from the device. Note that the angular range of the far-field pat-
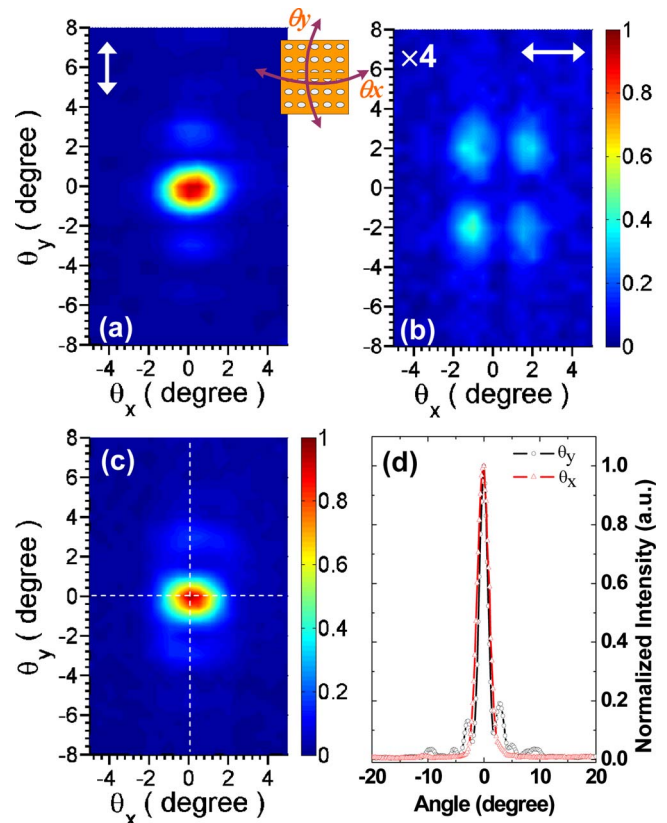

Fig. 2. (Color online) Far field measured at 78 K in pulsed mode (50 ns at 84 kHz). (a), (b) far-field patterns measured with a linear polarizer placed in front of the detector in θy and θx directions, respectively. The intensity of the pattern shown in (b) is multiplied by a factor of 4. The arrows show the polarization direction, and the inset defines the scan directions. The angular resolution is 0.5 deg. The sample-to-detector distance is 15 cm. (c) 2D unpolarized scan of the far-field pattern. The dashed curves correspond to θ_x and θ_y axes. (d) 1D unpolarized scan of the far-field pattern along the θ_x and θ_y axes with an angular resolution of 0.2 deg.

terns is small; therefore the θ_x and θ_y axes can be assumed approximately parallel to the x and y axes of the PhC. The θ_y-polarized far-field pattern shows an intense main lobe with two very weak side lobes. The θ_x-polarized pattern shows instead four extremely weak lobes, and no field is detected along the θ_y and θ_x axes. We have therefore obtained linearly polarized surface emission with a single-lobed emission pattern. In particular, the degree of polarization—defined as $I_{max}(E_y)/I_{max}(E_x)$—is $\asymp 8.0$, and the integrated intensity of the θ_y-polarized field is about 2.5 times the θ_x-polarized field. Here, $I_{max}(E_x)$ or $I_{max}(E_y)$ stands for the maximum of θ_x- or θ_y-polarized field in the far field. In fact, the unpolarized far-field pattern [Fig. 2(c)] is essentially identical to the θ_y-polarized pattern. Finally, 1D sections of the unpolarized far-field pattern across the θ_x and θ_y axes are shown in Fig. 2(d). The main-to-minor lobe-intensity ratio is ~5, and the FWHM of the emission cone is 2.4° $\times$ 1.8°, which is almost the diffraction-limited spreading angle.

The numerical simulations support the experimental findings. Figures 3(a) and 3(b) show respectively
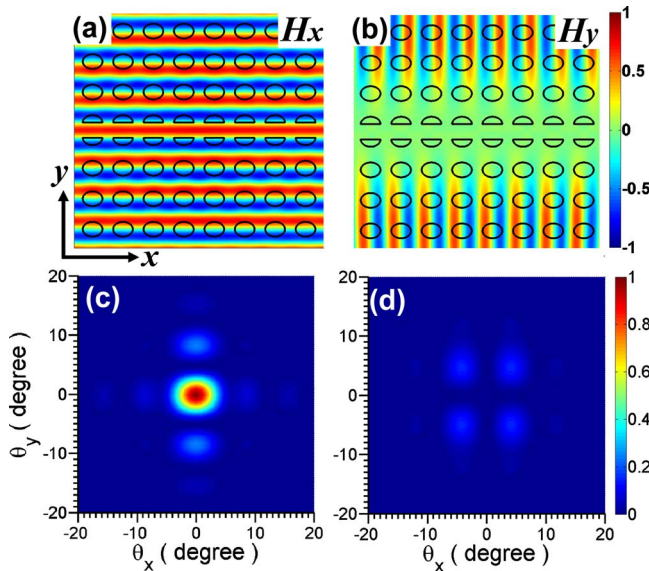
Fig. 3. (Color online) (a), (b) Central parts of the calculated distributions of H_x and H_y in the x–y plane. (c) and (d) The calculated far-field patterns $|E_{y,far}|^2$ and $|E_{x,far}|^2$, respectively.

the distribution of H_x and H_y in the x–y plane, calculated by 2D finite-difference time-domain approach [12]. The simulation domain is set to 40 periods in both directions. The effective indexes of the regions with and without air holes are—respectively—3.14 and 3.24, estimated by 1D calculation. The amplitude of H_x is dominant with respect to H_y. In fact, when the air holes are elliptical, the symmetry of the PhC decreases from a fourfold to a twofold rotation symmetry. Hence the balance between H_x and H_y is broken, leading to polarized emission [6]. Furthermore, the π phase shift reverses the field symmetry with respect to the y direction [9]. The dominant TM field (H_x) becomes symmetric in both x and y directions, thus leading to single-lobed surface emission.

Figures 3(c) and 3(d) report the calculated time-averaged intensity of the electric field $|E_{y,far}|^2$, and $|E_{x,far}|^2$, in the far field. They correspond to the measured far-field patterns polarized in the θ_y and θ_x directions, respectively, and they are calculated by means of near-to-far-field Fourier transformation [13]. Only the fields in the air holes are used to calculate the far-field pattern, because in the mid-IR the electromagnetic field cannot penetrate through the thick metallic layers (Ti/Au, 3 nm/80 nm) of the top metallization. This strategy has been recently applied with success [9,14]. The far fields strongly depend on the polarization. The integrated intensity of $|E_{y,far}|^2$, is about 2.3 times that of $|E_{x,far}|^2$, mainly determined by the holes eccentricity, in excellent agreement with the experiment. Figure 3(c) shows that $|E_{y,far}|^2$ exhibits one high-intensity lobe and two weak side lobes. This is because H_x is symmetric in both directions; hence the constructive interference confines $|E_{y,far}|^2$ in the center of the far field. The two side

lobes correspond to the second-order diffraction maxima, whose intensity is determined by the envelope of H_x in the near field. Figure 3(d) demonstrates that $|E_{x,far}|^2$ has four very weak lobes, while no field is apparent along the θ_x and θ_y axes, in excellent agreement with the experiment. This is again a consequence of the antisymmetry of H_y with respect to both the x and y axes [Fig. 3(b)]. Note that not only is the *shape* of the far field in excellent agreement with the experiment, but also its *quantitative details*. For instance, the theoretical degree of polarization is about 9, while we measure about 8.

In summary, we have reported single-mode, surface-emitting, mid-IR PhC QCLs with linearly polarized emission and well-behaved far fields. Future efforts will focus on implementing matrices of surface emitters for applications and—as a prerequisite—achieving pulsed, room-temperature operation.

References

1. D. Hofstetter, J. Faist, M. Beck, and U. Oesterle, Appl. Phys. Lett. **75**, 3769 (1999).
2. E. Mujagic, C. Deutsch, H. Detz, P. Klang, M. Nobile, A. M. Andrems, W. Schrenk, K. Unterrainer, and G. Strasser, Appl. Phys. Lett. **95**, 011120 (2009).
3. Y. Chassagneux, R. Colombelli, W. Maineult, S. Barbieri, H. Beere, D. Ritchie, S. P. Khanna, E. H. Linfield, and A. G. Davies, Nature **457**, 174174–178 (2009).
4. G. Xu, V. Moreau, Y. Chassagneux, A. Bousseksou, R. Colombelli, G. Patriarche, G. Beaudoin, and I. Sagnes, Appl. Phys. Lett. **94**, 221101 (2009).
5. M. Imada, S. Noda, A. Chutinan, T. Tokuda, M. Murata, and G. Sasaki, Appl. Phys. Lett. **75**, 316 (1999).
6. S. Noda, M. Yokoyama, M. Imada, A. Chutinan, and M. Mochizuki, Science **293**, 1123 (2001).
7. G. Witjaksono and D. Botez, Appl. Phys. Lett. **78**, 4088 (2001).
8. E. Miyai and S. Noda, Appl. Phys. Lett. **86**, 111113 (2005).
9. Y. Chassagneux, R. Colombelli, W. Maineult, S. Barbieri, S. P. Khanna, E. H. Linfield, and A. G. Davies, Appl. Phys. Lett. **96**, 031104 (2010).
10. M. Bahriz, V. Moreau, J. Palomo, R. Colombelli, D. A. Austin, J. W. Cockburn, L. R. Wilson, A. B. Krysa, and J. S. Roberts, Appl. Phys. Lett. **88**, 181103 (2006).
11. A. Bousseksou, V. Moreau, R. Colombelli, C. Sirtori, G. Patriarche, O. Mauguin, L. Largeau, G. Beaudoin, and I. Sagnes, Electron. Lett. **44**, 807 (2008).
12. A. Farjadpour, D. Roundy, A. Rodriguez, M. Ibanescu, P. Bermel, J. P. Joannopoulos, S. G. Johnson, and G. Burr, Opt. Lett. **31**, 2972 (2006).
13. J. Vuckovic, M. Loncar, H. Mabuchi, and A. Scherer, IEEE J. Quantum Electron. **38**, 850 (2002).
14. Y. Chassagneux, R. Colombelli, W. Maineult, S. Barbieri, S. P. Khanna, E. H. Linfield, and A. G. Davies, Opt. Express **17**, 9491 (2009).